

Performance Evaluation of Hypersonic Intake for Scramjet Engine

Sunil Kumar.S¹, Pranay Pandey², Juluru Sandeep³

Hindustan Institute of Technology and Science, Chennai

FOSSEE, IIT – Bombay

Institute of Aeronautical Engineering, Hyderabad

Abstract

Hypersonic intake performance is governed by complex flow physics, shock-boundary layer interactions and flow separation phenomena, which strongly influence key performance parameters such as total pressure recovery, mass capture and overall propulsion efficiency. Accurate numerical simulation supported by experimental investigations are therefore essential for reliable analysis and optimization of the intake designs for scramjet operations. In the present study, a reference intake geometry reported by Idrish et al. is investigated using OpenFOAM v2506. The simulations are carried out using the density -based solver rhoCentralFoam, coupled with the SST $k - \omega$ turbulence model, to accurately capture shock structures and viscous effects. The Computational setup is designed to closely recreate the simulation and experimentally analysed intake configuration, while using the flexibility of OpenFOAM solver and discretization schemes options. The study also incorporates the analysis of the intake with off-design condition along with the comparative analysis of Ansys Mesh and the OpenFOAM - BlockMesh utility. The numerical results show good agreement with the reference data, with deviation of 15%, demonstrating the capability of the chosen solver-model framework for hypersonic intake flow prediction and performance assessment.

Keywords: BlockMesh, OpenFOAM, rhoCentralFoam, Boundary Layer.

1. Introduction

Supersonic combustion ramjet (scramjet) technology is widely regarded as a key enabler for future high-speed air-breathing vehicles intended for access-to-space, long-range strike, and rapid global transport missions. Scramjet engines are attractive because they can utilize atmospheric oxygen as the oxidizer, reducing onboard propellant mass and potentially improving overall system efficiency compared with purely rocket-based concepts. Hypersonic intakes form the front-end of these propulsion systems and play a decisive role in determining engine performance, operability, and structural loading by shaping how the incoming hypersonic stream is captured, compressed, and delivered to the combustor (Saha & Chakraborty, 2012).

The overall performance of scramjet and ramjet engines is strongly governed by inlet efficiency, since the engine depends on the quantity and quality of the captured mass flow to generate stable thrust. The intake must provide sufficient compression to raise static pressure and temperature to levels compatible with supersonic combustion, while at the same time minimizing total-pressure losses and avoiding excessive drag penalties. In this context, various hypersonic intake configurations have been developed, including Internal, External and Mixed Compression inlet (fig1,2&3). Each offering different trade-offs between pressure recovery, starting characteristics, structural complexity, and integration with the airframe (Jagadish Babu et al., n.d.).

In a typical scramjet engine installation, the intake is responsible for decelerating and compressing the freestream hypersonic air through a series of oblique shocks and, in some cases, a terminal shock located upstream of the isolator (Saha & Chakraborty, 2012). This process generates the high static pressure and temperature required for efficient supersonic combustion, but must be managed carefully to avoid large total-pressure losses that directly degrade mass flow rate of the intake (Sandeep & Gupta, 2025). The flow delivered to the isolator and combustor should be as uniform as possible in terms of Mach number, pressure, and temperature, because strong non-uniformities can lead to combustion instability, structural hot spots, and adverse interactions between the intake, isolator, and combustor that may trigger engine unstart.

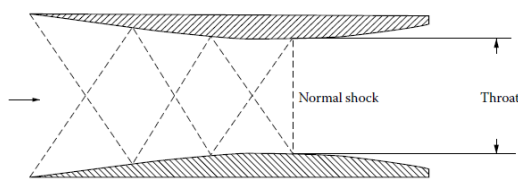


Figure 1: Internal compression Intake.

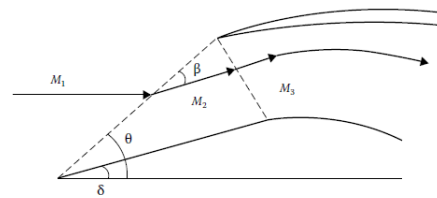


Figure 2: External-Compression Intake

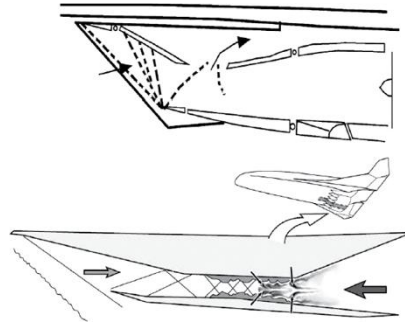


Figure 3: Variable- and fixed-geometry intakes.

From a fluid-dynamic standpoint, hypersonic intakes exhibit highly complex internal flow fields characterized by strong shock systems, shock–boundary-layer interactions, possible separation pockets, and three-dimensional sidewall effects (Idris et al., 2014). These phenomena have a major impact on key performance indicators such as mass capture ratio, total-pressure recovery, kinetic energy efficiency, and exit-plane flow uniformity. The operational envelope of an intake is typically described in terms of its starting and unstating behaviour across variations in Mach number. Unstart events are associated with large-scale separations and upstream motion of the internal shock system, leading to a sudden reduction in captured mass flow and pressure recovery, which can severely impair or even disrupt engine operation.

A persistent design challenge is to achieve robust starting characteristics and stable operation over a broad flight envelope while maintaining high total-pressure recovery and low drag. Mixed-compression intakes, which combine external and internal compression, are often favoured for their high pressure-recovery potential and good combustor matching, but they are particularly vulnerable to boundary-layer growth, back-pressure fluctuations, and geometric imperfections (Saha & Chakraborty, 2012). Consequently, current research trends focus on advanced flow-control strategies such as boundary-layer bleed, variable-geometry ramps and cowl, and active or passive devices (including suction, blowing, and plasma-based concepts) to mitigate shock-induced separation and reduce the likelihood of unstart or buzz. In parallel, CFD-driven multi-objective optimization and surrogate-based design methods are increasingly employed to systematically explore large design spaces, balancing competing objectives such as maximizing pressure recovery and minimizing drag, while preserving acceptable starting margins and robustness to disturbances (Jagadish Babu et al., n.d.).

2. Literature Review on Hypersonic Intake CFD Analysis

2.1 Idris et al. (2014) - Experimental Benchmark

Idris et al. conducted cold-flow experiments on a generic two-ramp scramjet inlet-isolator at Mach 5 in a high-supersonic tunnel, using pressure-sensitive paint (PSP) for global surface pressure mapping alongside Kulite transducers and color schlieren. The design targeted shock-on-lip (SoL) at zero angle-of-attack (AoA) but deliberately violated shock-on-shoulder (SoS) to satisfy Kantrowitz self-start criteria, resulting in shoulder separation, cowl-tip separation, and third isolator separation bubbles forming a "background wave" precursor to shock trains. PSP revealed Type 5 off-design interactions at the cowl tip and Edney Type II Mach stems at $\text{AoA}=4^\circ$, with performance improving at modest AoA (2° - 4°): total pressure efficiency rose from 0.32 to 0.46, kinetic energy efficiency from 0.92 to 0.95, and compression ratio from 17.7 to 38.7, though $\text{AoA}=4^\circ$ introduced subsonic pockets raising static temperature by 30 K. Wall pressures matched CFD (SST $k-\omega$) within 6%, confirming PSP's utility for non-intrusive diagnostics, while spanwise uniformity (std. dev. $<5.5\%$ except $\text{AoA}=4^\circ$ exit at 8.1%) validated 2D assumptions.

2.2 Sandeep et al. (2024) - CFD Validation and Off-Design Extension

Sandeep et al. modified the Idris geometry in ANSYS Fluent (RANS, SST $k-\omega$) to enforce SoS via isolator height reduction (6.8 mm to 4.7 mm), achieving inviscid shock patterns matching analytics (pressure ratios ~ 39 -44) but viscous simulations showed unstart due to excessive contraction and separation bubbles blocking supersonic flow. Off-design analysis at Mach 4-8, AoA -5° to 10° , and altitudes 29-32 km revealed total pressure recovery dropping from 15% (Mach 5) to 1% (Mach 8), normalized pressure ratio rising from 19 to 72, and separation bubble growth to 70% isolator height; real-gas effects at altitude boosted exit velocity from 600 m/s (wind tunnel) to 1200 m/s. Diamond-shaped injectors at 45° (9 units, $<4\%$ mass flow) suppressed bubbles from 4 mm to 0.95 mm at Mach 5, enhancing recovery by 22% and reducing drag via vortex mixing, outperforming circular/square/rectangular/triangular orifices.

2.3 Saha & Chakraborty (2012) - CFD Starting Characteristics

Saha & Chakraborty validated 3D RANS (SST $k-\omega$) simulations against Emami-Trexler experiments for a mixed-compression intake (11° ramp, 3° cowl) at Mach 3-8, capturing ramp pressures, mass capture ratios, and total pressure recovery within experimental scatter. Unstart occurred via sudden mass capture drop (e.g., Mach ~ 3 isothermal, ~ 4 adiabatic), driven by large entrance separation bubbles from shock-boundary layer interaction (SBLI); adiabatic walls (higher recovery temperature ~ 900 K) reduced boundary layer momentum, promoting earlier unstart vs. isothermal (300 K). Fine grids sharpened shock reflections; separation onset traced via zero wall shear, with dual bubbles at Mach 4 causing spillage and expulsion.

2.4 Jagadish Babu et al. (2016) - Parametric Inviscid Study

Jagadish Babu et al. performed inviscid Euler simulations on a two-ramp mixed-compression intake designed for Mach 6.5 (shock-on-lip, cowl shock cancellation at shoulder), varying Mach 4.5-7.5, AoA $\pm 6^\circ$, and cowl deflection 0° - 9° . On-design yielded 30.5 static pressure ratio and 0.52 total pressure recovery; off-design showed spillage at lower Mach (reduced capture area), isolator shock/expansion trains at higher Mach, with kinetic energy efficiency peaking at design (0.99) but dropping due to

stronger shocks or spillage. Positive AoA increased capture/mass flow but degraded recovery; cowl deflection reduced mass flow linearly while shifting peak efficiency to lower Mach.

3. Problem Definition

The present study is motivated by the need to exploit modern open-source CFD tools to perform high-fidelity analysis of hypersonic intake flows and to assess their capability to reproduce experimentally observed flow physics. OpenFOAM v2506, an open-source finite-volume CFD framework, offers a flexible platform for simulating compressible, turbulent, high-speed flows using customized numerical schemes, turbulence closures, and boundary conditions tailored to hypersonic applications. Leveraging this framework enables detailed investigations without the licensing constraints associated with commercial solvers, while still providing access to advanced discretization methods and parallel computing capabilities suitable for three-dimensional intake configurations.

A central objective of this work is to numerically replicate a reference hypersonic intake configuration documented in the literature (Idris et al., 2014) and evaluate the extent to which OpenFOAM-based simulations can capture the key flow features observed in experimental measurements. By carefully matching geometry, inflow conditions, and relevant non-dimensional parameters, the study aims to determine if the chosen numerical models and turbulence closures can accurately reproduce shock structures, separation patterns, pressure distributions, and exit-plane flow characteristics described in the reference experiments. Demonstrating such agreement is crucial to establish confidence in using open-source CFD for predictive hypersonic intake design.

Also, this study focuses on the performance of the hypersonic intake at off-design conditions, a critical consideration since in real flight scenarios the vehicle operates across a range of Mach numbers rather than a single design point. The inlet design is closely tied to a specific Mach number, but it must also efficiently handle flow at velocities deviating from this nominal value. When freestream velocity falls below the design Mach number, shocks produced by ramps converge upstream of the cowl lip, causing flow spillage, increased drag, and reduced mass flow capture. Conversely, at velocities above the design value, shocks are pushed further inside the inlet, potentially causing flow detachment and distortion, which degrade performance and may lead to unstable operations such as unstart phenomena. This sensitivity to off-design conditions necessitate detailed study across the flight envelope to ensure intake robustness and operability.

Integrating this focus enables deeper insights into shock dynamics, flow separations and pressure recovery effects under off-design conditions-phenomena especially significant for mixed-compression intakes that, while excelling at design speeds are more susceptible to disturbances due to complex shock band boundary layer interactions. Accurately capturing these behaviours in Open FOAM v2506 simulations will validate the numerical models' predictive capabilities and support the design of more resilient and efficient hypersonic intake systems capable of stable operation over a wide range of flight conditions.

4. Governing Equations

The hypersonic intake flow is modelled using the Compressible Navier-Stokes equations for a calorically perfect gas. The system consists of the continuity, momentum, and total energy equations.

Continuity Equation

$$\frac{\partial \rho}{\partial t} + \nabla \cdot (\rho u) = 0 \quad (1)$$

Momentum Equation

$$\frac{\partial}{\partial t}(\rho u) + \nabla \cdot (\rho u u) = -\nabla p + \nabla \cdot \tau \quad (2)$$

Viscous Stress Tensor

$$\tau = \mu \left[\nabla u + (\nabla u)^T - \frac{2}{3} \mu (\nabla \cdot u) I \right] \quad (3)$$

Total Energy Equation

$$\frac{\partial}{\partial t}(\rho E) + \nabla \cdot [(\rho E + p)u] = \nabla \cdot (k \nabla T) + \nabla \cdot (\tau \cdot u) \quad (4)$$

Where

$$E = e + \frac{1}{2} |u|^2 \quad (5)$$

Equation of State (Perfect Gas)

$$p = \rho R T \quad (3)$$

Or in total energy form:

$$e = \frac{p}{(\gamma - 1)\rho} \quad (4)$$

Total Energy per Unit mass

$$E = e + \frac{1}{2} (u^2 + v^2 + w^2) \quad (5)$$

Total Energy per Unit Volume (used in CFD solvers like rhoCentralFoam, hy2Foam, rhoPimpleFoam)

$$\rho E = \rho e + \frac{1}{2} \rho (u^2 + v^2 + w^2) \quad (9)$$

Total Pressure (Isentropic, ideal gas)

$$p_0 = p \left(1 + \frac{\gamma - 1}{2} M^2 \right)^{\frac{\gamma}{\gamma - 1}} \quad (6)$$

Total Pressure Recovery

$$\pi = \frac{p_{0,2}}{p_{0,1}} \quad (7)$$

Here 1 and 2 refer to the upstream (2) and downstream (1) location where the total pressure values being calculated.

Temperature-dependent viscosity is computed using Sutherland's law:

$$\mu(T) = \mu_0 \left(\frac{T}{T_0} \right)^{3/2} \frac{T_0 + S}{T + S} \quad (8)$$

5. Turbulence Modelling

This study uses SST $k - \omega$ Turbulence Model developed by **F. R. Menter**, is one of the most widely used two-equation RANS turbulence models for high-speed aerodynamic applications. It combines the advantages of both the standard $k - \omega$ model (accurate near-wall treatment) and the $k - \epsilon$ model (robust free-stream behaviour) using a blending function approach. This hybrid formulation makes SST SST $k - \omega$ particularly well-suited for flows involving strong adverse pressure gradients, shock–boundary layer interactions, flow separation, and high-speed compressible effects, all of which are dominant in hypersonic intake systems.

Reynolds-averaged continuity and momentum (incompressible / low-Mach RANS form)

$$\frac{\partial \rho}{\partial t} + \frac{\partial}{\partial x_j} (\rho U_j) = 0 \quad (9)$$

$$\frac{\partial}{\partial t} (\rho U_i) + \frac{\partial}{\partial x_j} (\rho U_i U_j) = -\frac{\partial p}{\partial x_i} + \frac{\partial}{\partial x_j} \left[(\mu + \mu_t) \left(\frac{\partial U_i}{\partial x_j} + \frac{\partial U_j}{\partial x_i} \right) \right] \quad (10)$$

5.1 SST $k - \omega$ transport equations

Turbulent kinetic energy k :

$$\frac{\partial(\rho k)}{\partial t} + \frac{\partial(\rho U_j k)}{\partial x_j} = P_k - \beta^* \rho k \omega + \frac{\partial}{\partial x_j} \left[(\mu + \sigma_k \mu_t) \frac{\partial k}{\partial x_j} \right] \quad (11)$$

Specific dissipation rate ω :

$$\begin{aligned} \frac{\partial(\rho \omega)}{\partial t} + \frac{\partial(\rho U_j \omega)}{\partial x_j} &= \alpha \frac{\omega}{k} P_k - \beta \rho \omega^2 + \frac{\partial}{\partial x_j} \left[(\mu + \sigma_\omega \mu_t) \frac{\partial \omega}{\partial x_j} \right] \\ &+ 2(1 - F_1) \rho \sigma_{\omega 2} \frac{1}{\omega} \frac{\partial k}{\partial x_j} \frac{\partial \omega}{\partial x_j} \end{aligned} \quad (12)$$

P_k is the production of turbulent kinetic energy:

The last cross-diffusion term in the $\omega -$ equation is the cross-diffusion introduced by Menter when blending from $k - \omega$ to a transformed $k - \epsilon$ formulation away from walls.

5.2 Production term P_k :

$$P_k = \tau_{ij} \frac{\partial U_i}{\partial x_j} \quad (13)$$

5.3 Eddy (turbulent) viscosity — SST limiter

The SST model uses a limiter for the eddy viscosity to account for transport of the turbulent shear stress:

$$\nu_t = \frac{a_1 k}{\max(a_1 \omega, S F_2)} \quad (14)$$

$$\mu_t = \rho \nu_t \quad (15)$$

where S is the strain-rate magnitude defined above, a_1 is a model constant, and F_2 is the second blending function.

Blending of coefficients

Coefficients are blended between two sets (near-wall “1” and far-field “2”) using F_1 :

$$\phi = F_1 \phi_1 + (1 - F_1) \phi_2 \quad (16)$$

so $\alpha, \beta, \sigma_k, \sigma_\omega, \dots$ are blended this way.

5.4 Blending functions F_1 and F_2

$$F_1 = \tanh \left(\left[\min \left(\max \left(\frac{\sqrt{k}}{\beta^* \omega y}, \frac{500 \nu}{y^2 \omega}, \frac{500 \nu}{y^2 \omega} \right), \frac{4 \sigma_{\omega 2} k}{C_{D_{k\omega}} y^2} \right) \right]^4 \right) \quad (17)$$

$$F_2 = \tanh \left(\left[\max \left(\frac{2\sqrt{k}}{\beta^* \omega y}, \frac{500 \nu}{y^2 \omega} \right) \right]^2 \right) \quad (18)$$

Thus, the blending function smoothly transitions between the near-wall and free-stream formulations, ensuring numerical stability and physical consistency across the boundary layer.

6. Computational Domain

The computational Domain is made as per the paper (Idris et al., 2014) and in order to reduce the shock reflection or any kind of abnormalities from the farfield that can be imposed on the wall section the computational domain is stretched 2.5 time longer in the y direction.

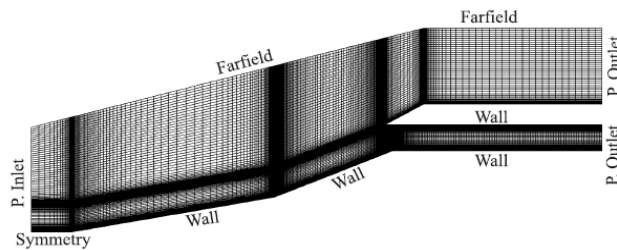


Figure 4: Reference Computational Domain

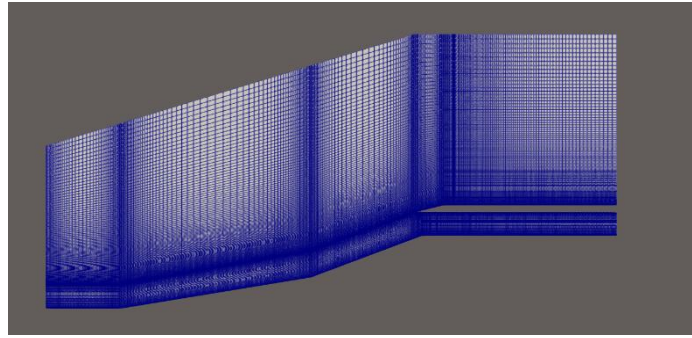


Figure 5: Simulation Computational Domain Made with Ansys Mesh

7. Meshing

The study present with 2 types of meshing done with BlockMesh utility from OpenFoam and Ansys meshing the reason will be explained in subsequent sections. Both the Mesh was made with a finer value to produce a Y^+ value of 1.

Ansys Meshing

The domain was split into 10 subdomain and were provided with proper bias system to make sure the mesh reach the desired orthogonality and aspect ratio along with the Y^+ value.

Blockmesh utility

With the blockmesh utility same kind of computational domain is made with the same 10 subdomains and made sure the variation between the ansys mesh and blcokmesh is not much with lesser error. The process was fully done with blockMesh alone and multigrading approach were used to acquire desired near wall distance.

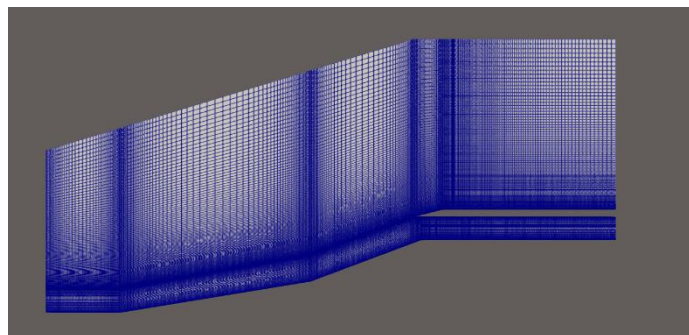


Figure 6:Computational Domain Made with Ansys Mesh

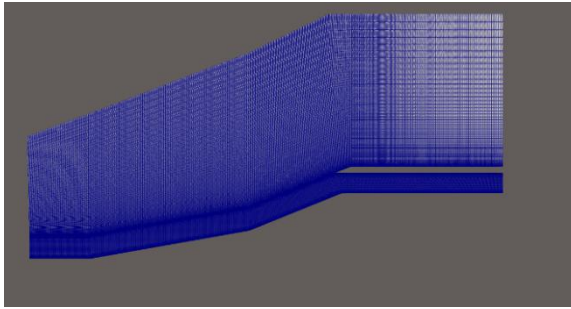


Figure 7: Computational Domain made with BlockMesh

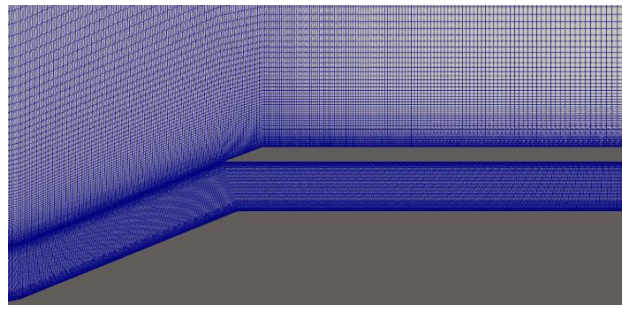


Figure 8: View of isolator section

The Mesh metric of both the BlockMesh and Ansys Meshing were provided in the below fig.9 & fig.10

```
Checking geometry...
Overall domain bounding box (-0.02 0 -0.00174539) (0.135 0.0802436 0.00174539)
Mesh has 2 geometric (non-empty/wedge) directions (1 1 0)
Mesh has 2 solution (non-empty) directions (1 1 0)
All edges aligned with or perpendicular to non-empty directions.
Boundary openness (-7.2528e-18 3.11847e-18 -1.37989e-19) OK.
Max cell openness = 5.27435e-15 OK.
Max aspect ratio = 137.65 OK.
Minimum face area = 6.60952e-10. Maximum face area = 7.8523e-06. Face area magnitudes OK.
Min volume = 2.30725e-12. Max volume = 1.08286e-08. Total volume = 3.0975e-05. Cell volumes OK.
Mesh non-orthogonality Max: 22.0012 average: 10.9166
Non-orthogonality check OK.
Face pyramids OK.
Max skewness = 0.815693 OK.
Coupled point location match (average 0) OK.

Mesh OK.
```

Figure 9: Mesh-Metric of Ansys Mesh

```
Checking geometry...
Overall domain bounding box (-0.0207 0 0) (0.135 0.0801 0.001)
Mesh has 2 geometric (non-empty/wedge) directions (1 1 0)
Mesh has 2 solution (non-empty) directions (1 1 0)
All edges aligned with or perpendicular to non-empty directions.
Boundary openness (1.81588e-17 -1.11967e-16 -2.06174e-13) OK.
Max cell openness = 1.15207e-15 OK.
Max aspect ratio = 70.1335 OK.
Minimum face area = 1.34239e-09. Maximum face area = 2.82801e-06. Face area magnitudes OK.
Min volume = 1.34239e-12. Max volume = 2.07944e-09. Total volume = 8.43249e-06. Cell volumes OK.
Mesh non-orthogonality Max: 25.6801 average: 11.6441
Non-orthogonality check OK.
Face pyramids OK.
Max skewness = 1.20832 OK.
Coupled point location match (average 0) OK.

Mesh OK.
```

Figure 10: Mesh Metric of blockMesh

8. Boundary and Initial Conditions

The simulation was done for Mach 5 as an initial case and with Mach 6,7,8 for off-Design Condition. The boundary Conditions used for the simulation are listed in the below table. The values for k, Omega and Epsilon are calculated with the Turbulence calculator from CFD Online with the desired inlet value for each case and it's also been provided in the table.

The initial value for Mach 5 had been taken from the reference paper

Note: All the value provided are static - Values

P – Pressure

- A fixed Static Pressure of 1228.52 Pa was applied at the inlet.
- At the Outlet, a WaveTransmissive boundary condition was used to allow non-reflective pressure waves, with $\gamma = 1.4$ and the Farfield reference pressure set to 1228.52 Pa.
- Walls were assigned a zero gradient conditions, while symmetry and Farfield patches used symmetry B.C..
- The front and back planes were set to empty

T -Temperature

- The inlet temperature was specified using a fixedvalue of 62.5K.
- A ZeroGradient conditions was applied at the outlet.
- The wall temperature was fixed at 300K, representing an isothermal surface.
- Symmetry and Farfield boundaries used symmetry conditions, and the front/back planes were defined as empty.

U – Velocity

- At the inlet, A freestreamVelocity condition was applied with a uniform velocity of 793.26 m/s
- The Outlet used an InlteOutlet Condition to allow smooth flow exit while preventing reverse inflow.
- Wall Boundaries were treated with the no-Slip condition.
- The Symmetry and Farfield patches used symmetry, and the front/back planes were set to empty.

Table 1: Boundary Conditions

Mach No.	Temperature	Pressure	Velocity	K	Epsilon	Omega
5	62.5	1228.525	793.256	23.60	7474.28	3518.96
6	45.73171	411.684	814.261	24.86	4463.32	1994.52
7	34.722	157.011	827.762	25.69	4688.84	2027.59
8	66.578	66.578	836.892	26026	4845.72	2049.96

9. Solver Selection

OpenFOAM v2506 provides 2 different types of solvers for high-Speed Compressible Flow solvers (Canteros & Polanský, 2024) –

- RhoCentralFoam – Density based Solver
- SonicFoam - Pressure based Solver

For this Study the Density based solver rhoCentralFoam was used with the turbulence Model SST-K-Omega. The study also provides a comparative assessment between the 2-solver providing the necessity for choosing one for the desired study. Both the solver the Boundary Conditions were taken as provided from the table. Since a Density based study was done in the reference paper the rhoCentralFoam was taken into prime consideration.

10. Discretization Schemes

A Tadmor Flux Scheme was used to provide robust shock capturing without relying on Reinmann solvers. This scheme ensures stable and non-oscillatory flux evaluation, which is essential for high-speed compressible flows with shocks and expansion waves.

Time Discretization (ddtSchemes)

The Euler scheme was applied for temporal discretization. This first-order explicit schemes provide numerical stability for Central Solver and is suitable for transient compressible simulations.

Gradient Schemes

- A Gauss linear gradient scheme was used to maintain second-order accuracy for gradient evaluation, ensuring smooth reconstruction of variables like velocity and temperature.
- Divergence Schemes
- Most divergence terms were disabled using default none to avoid undesired numerical dissipation in Central differencing.
- Specific Transport variables Variables (e.g., k , ω , ϵ , ν Tilda) used Gauss Gamma schemes, which introduces controlled numerical damping to prevent oscillations in Turbulence quantities, improving stability in high-gradient regions.

Laplacian Schemes

- A Gauss linear corrected scheme was adopted to ensure accurate diffusion terms, accounting for mesh non-orthogonality. This improves solution quality on unstructured grids.

Interpolation Schemes

- A linear interpolation scheme was used as the default for second-order accurate reconstruction.
- Gamma/Gamma_v reconstruction schemes for p,U and T improve boundedness and reduce numerical oscillation, which is important in shock-dominated flows.

Surface-Normal Gradient (snGrad) schemes

- A corrected scheme was applied to handle non-orthogonal meshes more accurately, reducing numerical errors in diffusion terms.
- Wall Distance Calculation
- The meshWave method was used for wall distance estimation, suitable for turbulence models that require accurate near-wall metrics.

Linear Solver – (fvSolution folder)

- Density, Momentum, and Energy (rho, rhoU, rhoE). These fields were solved using a diagonal solver, which is computationally efficient for the hyperbolic nature of the Central Differencing equations used in rhoCentralFoam.
- Fields such as U, e, h, k, ϵ , ω , vTilda were solved using the smoothSolver with Gauss-seidel smoothing and strict tolerances (10^{-10} to 10^{-12}). This provides fast convergence and numerical smoothness.
- Zero relative tolerance (relTol = 0) ensures that each equation is solved fully at every iteration.
- Multiply smoothing sweeps improve the stability of turbulence variable, especially in shock-Layer regions.

11. Implementation in OpenFOAM

OpenFOAM v2506 was utilised for the simulation and the case structure tree is provided as below

Case Set-Up Structure:

The case file consists of 3 folder 0, Constant and System under which the control variable, Mesh, Boundary Conditions and schemes files were placed. The below fig .11 and 12 ides the case file setup:

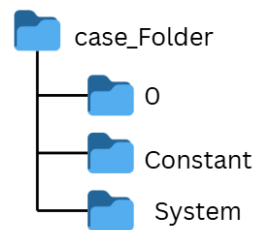


Figure 11: Case folder tree

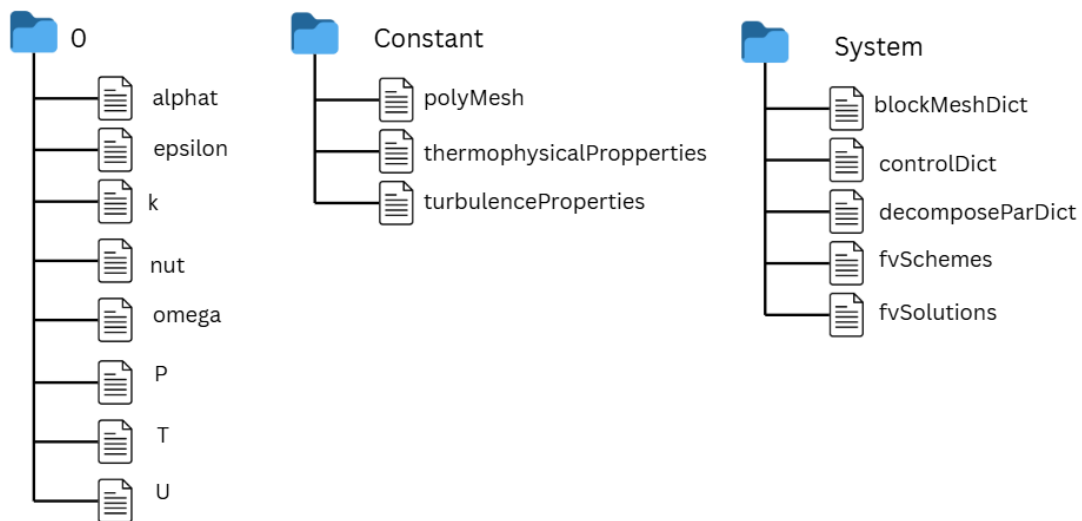


Figure 12: Folders from each subsection of the case file – 0, constant & System

11.1 Thermophysicalproperties

The simulation uses the hePsiThermo thermodynamic model with the perfect gas equation of state, which is appropriate for high-speed air flows where density varies strongly with temperature and pressure. A content-property (hConst) formulation is adopted for specific heat, viscosity and thermal conductivity, providing a stable and computationally efficient representation for compressible aerodynamic cases. Air is modelled as pure mixture with a molecular weight of 28.9 g/mol, constant $C_p = 100 \text{ J/kg-k}$, Viscosity $\mu = 1.8 \times 10^{-5} \text{ kg/m-s}$, and

Prandtl number of 0.7, which are standard values for calorically perfect air in high-speed flow simulations.

11.2 TurbulenceProperties

A Reynolds-Averaged Simulation (RAS) framework was used with the $k-\omega$ SST turbulence model, which blends the advantages of both $k-\epsilon$ and $k-\omega$ formulations and performs reliably in flows with strong adverse pressure gradients, shock-boundary layer interactions, and separated regions.

11.3 Control Dictionary

- Solver Selection – The case uses rhoCentralFoam, a density-based solver well suited for supersonic and hypersonic compressible flows with shocks
- Start and End Times – The simulation begins at $t=0$ and runs up to 0.00013s, sufficient to capture transient shock development and flow stabilization.
- Time-Step Size – An initial $\Delta t = 1 \times 10^{-8}$ s is used to ensure stability in regions with steep gradients, especially during the early shock formation.
- Automatic Time-Step Adjustment – adjustTimeStep yes with maxCo = 0.5 allows the solver to dynamically choose a stable timestep, maintaining a Courant number below 0.5.
- Maximum Allowed Time_step : maxDeltaT = 1 provides an upper limit, ensuring the timestep does not go beyond stable values.
- Write Controls: Output is written every 0.00001s, offering high temporal resolution for post-processing shock movement and transient features.
- Output Format: ASCII format with fixed precision ensures readable and consistent data for analysis.

12. Simulation Procedure

The simulation was executed in parallel using 8 processor cores, with the scotch decomposition method applied for optimal load balancing. The overall workflow followed the standard OpenFOAM parallel-run procedure and is summarized below:

1. Mesh Generation / Import
 - `blockMesh` – used when generating a structured mesh within OpenFOAM.
 - `fluentMeshToFoam` -used when converting an ANSYS Fluent mesh into an OpenFOAM readable format.
2. Mesh Quality Verification
 - `checkMesh` – performed to ensure the mesh meets the required quality criteria.
3. Domain Decomposition
 - `decomposePar` – decomposes the computational domain into 8 subdomains for parallel execution.
4. Running the Simulation in Parallel
 - `mpirun -np 8 rhoCentralFoam – parallel | tee log.rhoCentralFoam` – Runs the solver across 8 cores and simultaneously logs the residuals for post-processing.
5. Reconstructing the Case (if required)
 - `mpirun -np 8 redistributepar -reconstruct -parallel -newTimes` : Reconstructs the decomposed fields back into a single case folder.
6. Residual Monitoring
 - `pyFoamPlotWatcher.py log.rhoCentralFoam –hardcopy –format-of-hardcopy=png`: This is used to plot the residual graph and save as PNG images for future assessment.

13. Results and Discussions

13.1 The two High Speed Solvers in OpenFOAM

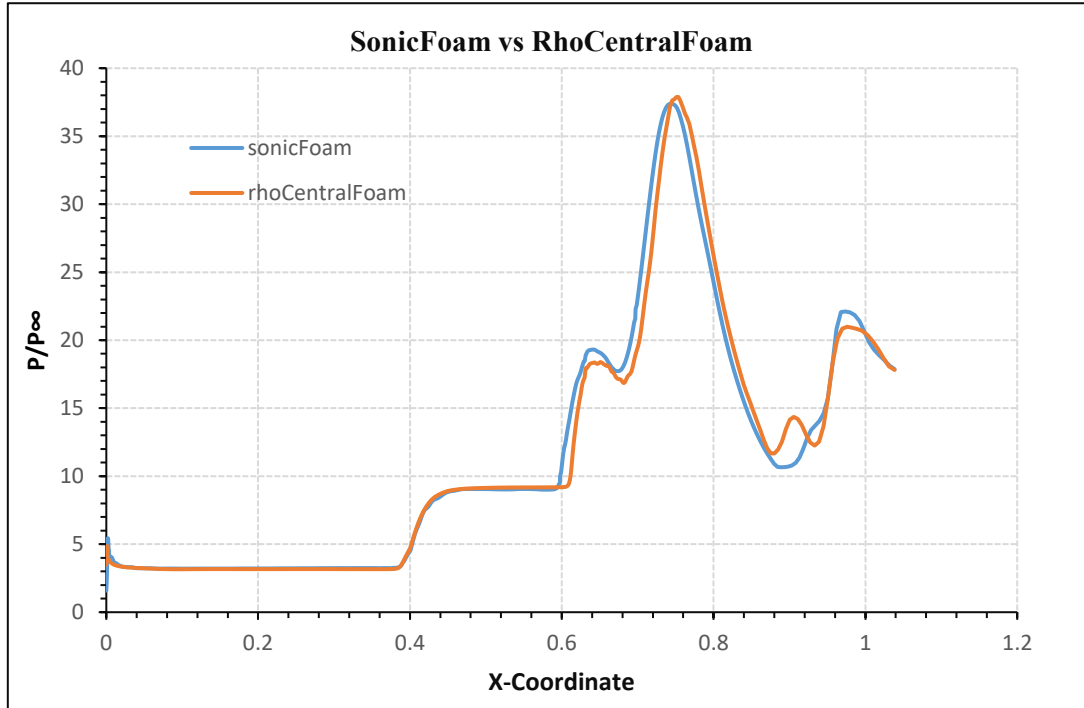


Figure 13: comparison plot of rhoCentralFoam and SonicFoam solvers

The pressure distribution along the intake wall predicted by SonicFoam and RhoCentralFoam shows overall good agreement in terms of shock Location and general pressure rise trends. Both the solver is capable of capturing the major hypersonic flow features. But the study made clear that besides the SonicFoam capability of resolving more or less all the features its being a pressure-based solver the shock reflection is now well captured compared to the rhoCentralFoam which is a density-based solver.

After the main pressure peak, both solvers predict a pressure drop; however, SonicFoam exhibits a deeper pressure undershoot, which may indicate increased sensitivity to expansion waves or shock-induced separation effects. On the whole rhoCentralFoam provides smoother pressure recovery compared to SonicFoam solver.

13.2 Results of BlockMesh and AnsysMesh

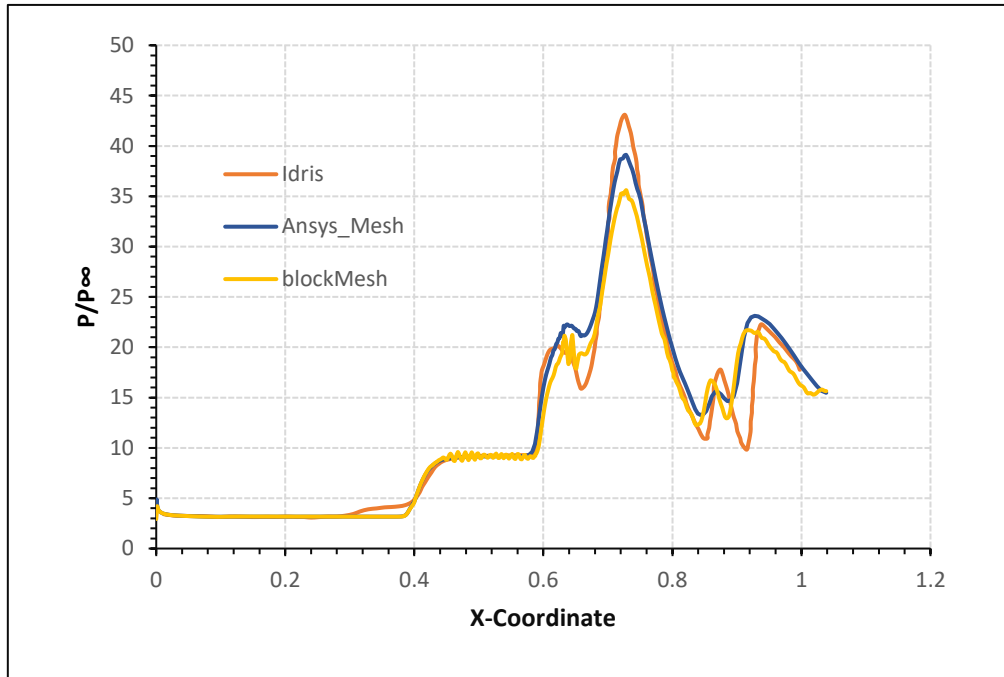


Figure 14: Comparative plot of BlockMesh and Ansys-Mesh

The above graph provides a detailed comparison of Meshing effects with reference to the results addressed by Idris et al. Two different Mesh generation approaches were evaluated – Ansys generated mesh and BlockMesh created using the OpenFOAM Utility. The Ansys follows the same trend as per the reference data, whereas the BlockMesh results show a lesser pressure ratio along with noticeable oscillatory behaviours. This behaviour is observed despite both meshes being constrained to a Y^+ value of 1.

A noticeable observation in the BlockMesh case is the stronger perdition of reflected shock and its associated effects, that more closely resembles the pattern reported by (Idris et al., 2014) across the downstream of the isolator region. In contrast the Ansys mesh is able to capture the presence of the reflected shock, the intensity is significantly weaker. The underlying cause of this irregularity is not fully understood however, it is likely to be a result of differences in mesh-metrices such as cell distribution, alignment and numerical dissipations characteristics inherent to each meshing strategy. Overall, despite the quantitative differences, both meshing approaches reproduces the trend observed in the reference results.

13.3. Validation

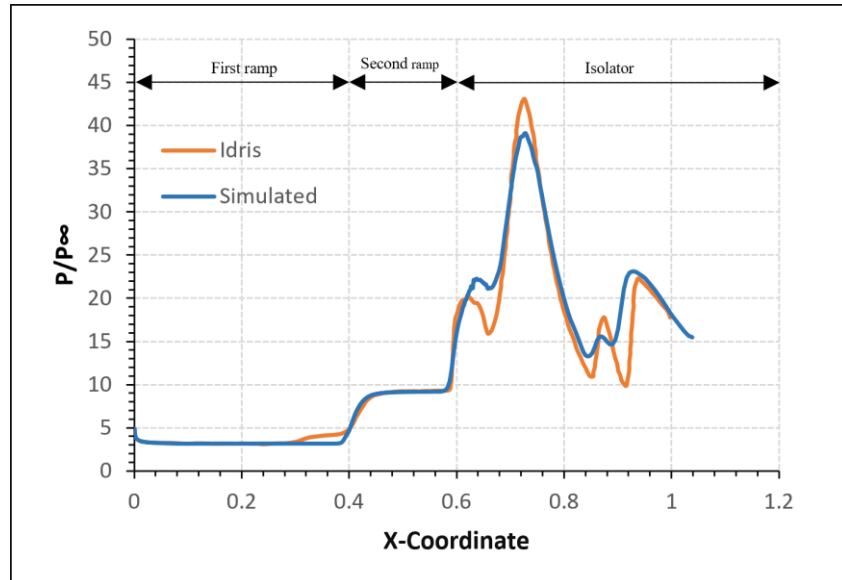


Figure 15: Simulated vs Idris paper

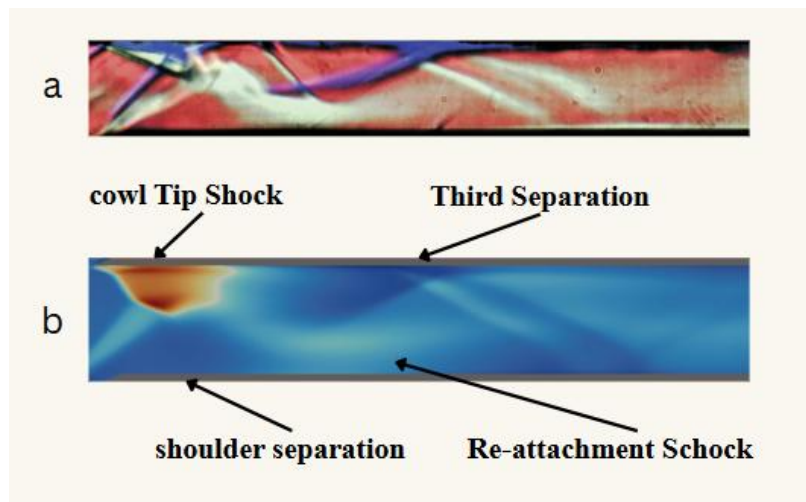


Figure 16: simulated view of the shock in comparison with experimental PSP view

In the 1st ramp region, both the simulated and reference results show a nearly constant pressure level, during the 2nd ramp a sharp rise in pressure is observed in both cases due to the formation of strong oblique shock. At the isolator entrance the simulated curve overpredicts thus exhibiting a distinct pressure peak, corresponding to shock coalescence and shock-shock interaction near the isolator entrance. The small shift in peak location suggests marginal

difference in shock reflection or numerical dissipation but remains within acceptable limits for high-speed intake simulations. In the isolator region the simulated result slightly underpredicts the strength of reflection shock downstream of the isolator this may be due to the pressure relaxation with the oscillatory behaviour.

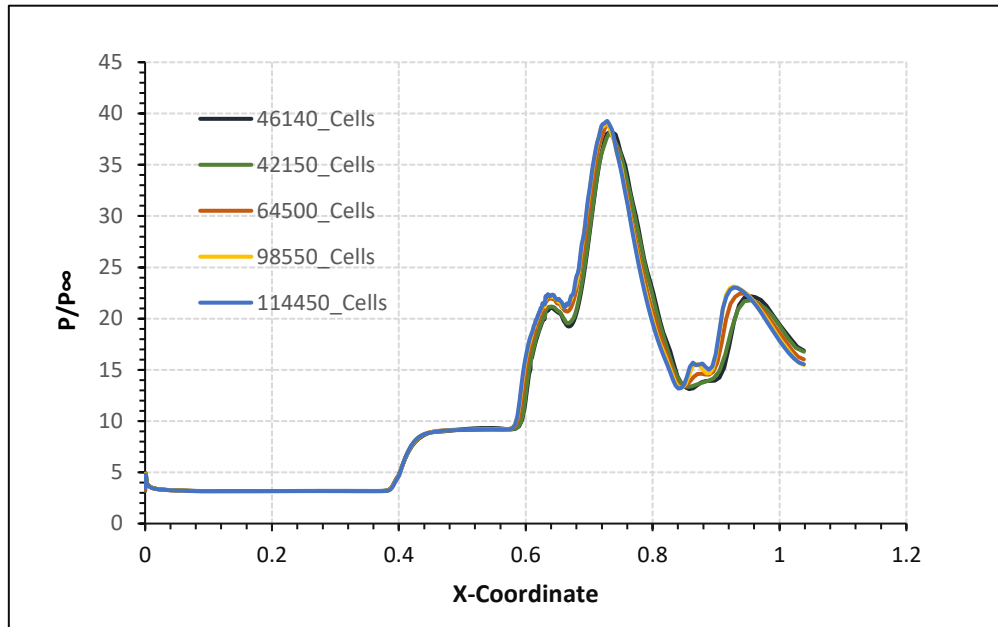


Figure 17: Grid Independence Study

The grid independence study presented in the above figure provides insight into the minimum mesh resolution required to accurately capture the dominant hypersonic flow features. From the pressure distribution trends, it is evident that meshes in the range of approximately 98k to 114k cells yield converged results, with no significant variation in the resolved shock structures and pressure peaks. Therefore, a mesh resolution within this range is recommended as it offers an optimal balance between numerical accuracy and computational efficiency.

The qualitative trends and key flow features are consistently reproduced the visual representation at the figure b provides a good aggregate of reflection shock formation similar to the (Idris et al., 2014) case. The discrepancies are primarily due to the combined effects of turbulence modelling with the solver used, producing numerical dissipations. And the effects observed were within an allowable limit of 15%.

The quantitative agreement between the simulated and reference data confirms the reliability of the numerical setup, including geometry, boundary conditions, and solver configuration.

13.4. Starting and Unstart Behaviour of the Hypersonic Intake

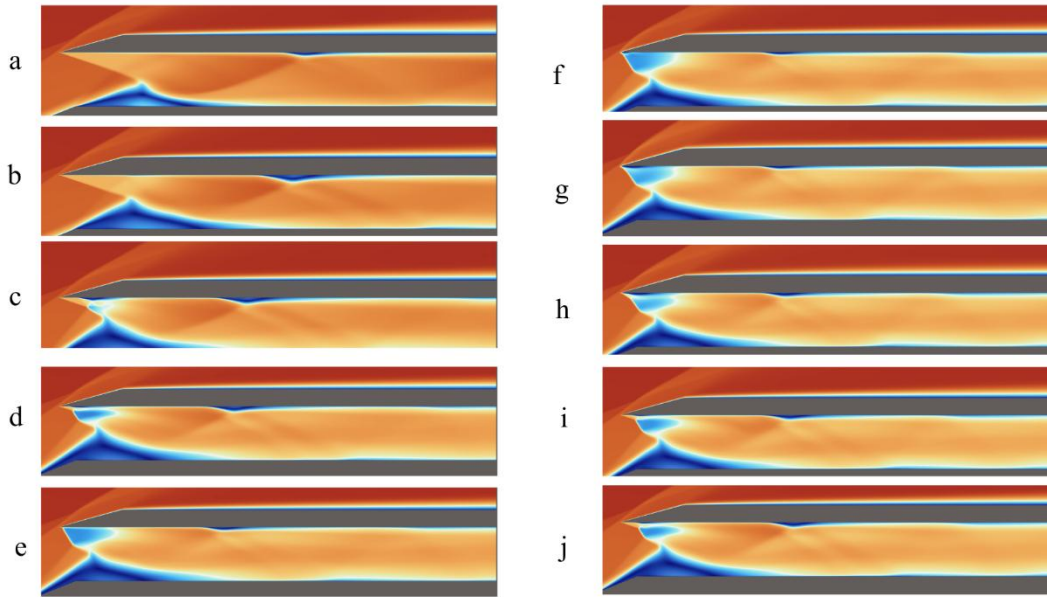


Figure 18: Shock Train Movement

- Figure (a–j) illustrates the evolution of the internal flowfield of the hypersonic intake operating at a free-stream Mach number of 5, highlighting the transition between started and unstarted flow regimes. In the initial cases (a–c), the intake exhibits a started condition, where the oblique shock generated at the intake lip is properly ingested and undergoes controlled reflection within the isolator. The shock system remains attached, allowing the supersonic core flow to be smoothly compressed while maintaining high Mach number throughout the duct. As the flow progresses downstream, a well-defined shock train develops, indicating stable pressure rise and effective flow swallowing by the intake.
- In intermediate cases (d–g), the intake approaches a marginally started state. Strengthening of the shock train and increased boundary-layer interaction led to localized flow deceleration and partial separation near the walls. The adverse pressure gradient intensifies, causing upstream movement of the shock system. This manifests as oscillatory shock positions and intermittent flow choking, signalling the onset of intake instability.
- In the later cases (h–j), a clear unstarted condition is observed. The shock system is expelled upstream of the intake throat, resulting in a strong normal or quasi-normal shock forming near or ahead of the inlet entrance. This leads to substantial total pressure loss, large subsonic regions within the duct, and severe flow separation along the walls. Consequently, the intake fails to swallow the required mass flow, and the internal compression mechanism collapses. These results clearly demonstrate the sensitivity of hypersonic intakes to shock–boundary layer interactions and back-pressure effects, emphasizing the critical role of isolator design and operating conditions in maintaining a stable started flow regime.

13.5. Mach Contours for varying Mach no. (5,6,7,8)

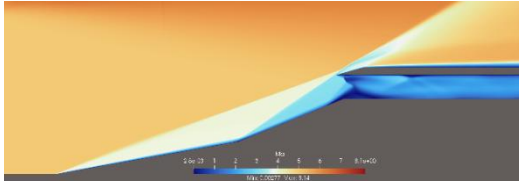


Figure 19: Mach 5

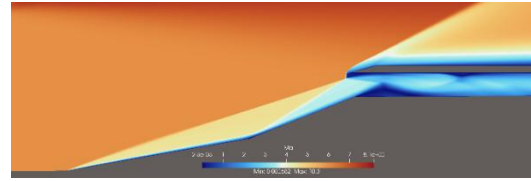


Figure 20: Mach 6

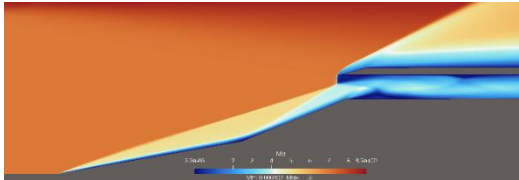


Figure 21: Mach 7

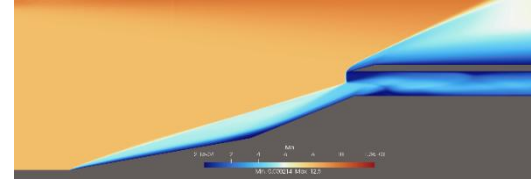


Figure 22: Mach 8

Density Contours for Varying Mach no. (5,6,7,8)

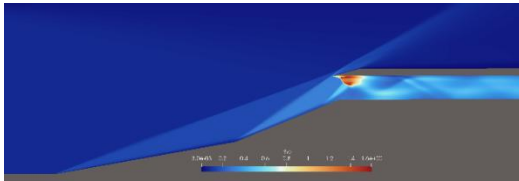


Figure 23: Mach 5

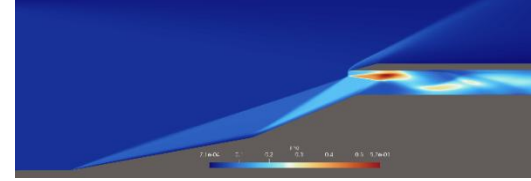


Figure 24: Mach 6

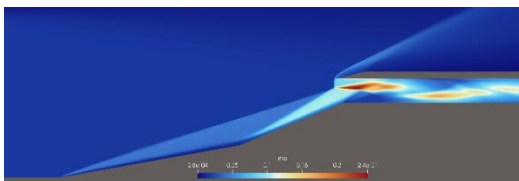


Figure 25: Mach 7

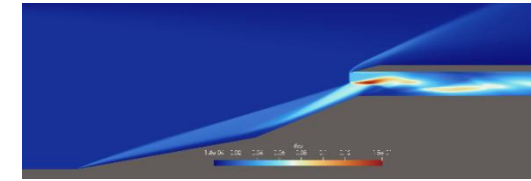


Figure 26: Mach 8

- Figures 19–22 present the Mach number contours for freestream Mach numbers ranging from Mach 5 to Mach 8. As the freestream Mach number increases, a clear strengthening of the oblique shock system generated at the leading compression surface is observed. At Mach 5, the shock is relatively weaker and attached closer to the compression ramp, allowing smoother flow compression and comparatively gradual deceleration. With increasing Mach number (Mach 6 and Mach 7), the shock angle decreases and the shock intensity increases, resulting in higher post-shock compression and a thicker shock layer near the ramp surface.
- At Mach 8, the shock becomes significantly stronger, leading to a pronounced rise in flow gradients near the compression corner. The interaction between the oblique shock and the boundary layer intensifies, causing an increase in low-Mach regions adjacent

to the wall, indicating enhanced viscous effects and potential flow separation tendencies near the compression ramp and downstream region.

- Figures 23–26 present the density contours corresponding to freestream Mach numbers 5, 6, 7, and 8, respectively. At Mach 5 (Figure 20), the density increase across the oblique shock is moderate, and the high-density region remains confined near the shock interaction zone. The density distribution downstream of the ramp is relatively uniform, suggesting stable compression with limited flow distortion.
- As the Mach number increases to Mach 6 and Mach 7 (Figures 24 and 25), a pronounced rise in post-shock density is observed. The high-density region expands downstream and closer to the wall, indicating stronger compression due to increased shock strength. The interaction between the shock and the boundary layer becomes more distinct, leading to localized density gradients and non-uniform flow structures in the downstream region.
- At Mach 8 (Figure 26), the density rise across the shock is substantial, with a well-defined high-density core forming immediately downstream of the compression corner. The density gradients are significantly sharper, and the downstream flow exhibits increased non-uniformity due to intensified shock interactions and boundary-layer effects. This behaviour highlights the severe compressibility effects encountered at higher hypersonic Mach numbers and their influence on intake flow stability and performance.

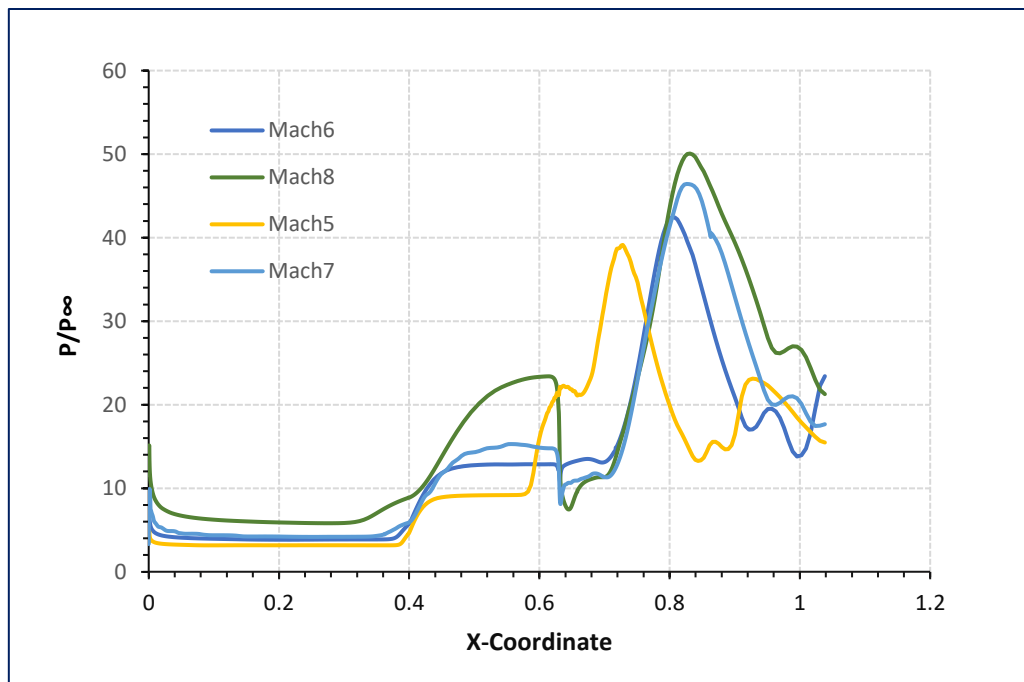


Figure 27: Pressure Ratio with varying Mach Number

Figure 27 represents a comparative analysis of the intake performance for varying freestream Mach no. (5,6,7 and 8). With an increase in Mach no., the shock train is observed to shift progressively downstream toward the isolator section, which is clearly indicated by the downstream movement of the peak locations in the graph. This downstream movement strongly relates to the phenomena of the Intake Unstart.

14. Conclusion

The results of the Case Study demonstrate the capability of OpenFOAM to accurately resolve the complex flow physics associated with Hypersonic Intakes for scramjet application – including SBLI and flow separation. The simulated results show good agreement with the reference data, with an overall error of 15%, validating the robustness of the adopted solver framework. However, the comparative study between the blockMesh and Ansys mesh reveals a nearly same results with numerical oscillation. But effective mesh generation using BlockMesh requires smaller time-step for a given Y^+ value of 1 which would require computationally more time to simulate. In comparison, meshes generated using Ansys offer improved computational efficiency while maintaining solution accuracy.

The selection of Numerical Schemes plays a critical role in capturing flow features, particularly the reflected shock train patterns downstream of the isolator section. Although more advanced robust schemes may be required for detailed resolution of these phenomena, the schemes employed in the present work provide a reliable baseline for accurately capturing the dominant flow physics. Furthermore, the off-design operating condition and transient simulations offer a border understanding of the evolution of flow separation regions and shock structures throughout the intake, highlighting the importance of unsteady analysis in Hypersonic intake performance evaluation.

15. Future Works

- The present study is limited to non-reactive flow analysis. For Mach no. exceeding 5, thermochemical nonequilibrium effects such as molecular dissociation become significant. Further investigations should incorporate reacting flow simulation to capture real gas effects.
- Such reacting flow simulations can be carried out using the reacting solvers available in OpenFOAM or alternatively with the extension of HyFoam solver, which is more suitable for accurately modelling high-enthalpy hypersonic flows.
- Further work is required to develop a more robust multi-gridding meshing strategy using the blockMesh utility, with particular emphasis on achieving desired wall Y^+ .
- Implementation of Adaptive Mesh Refinement (AMR) strategy is recommended to dynamically refine regions with strong gradients resulting in reducing overall computational cost while maintain solution accuracy.
- Further investigations into the selection of Discretization Methods and Flux scheme should be done thereby a clear understanding of the shock capturing process can be achieved

16. References

1. Canteros, M. L., & Polanský, J. (2024). Review and comparison of two OpenFOAM® solvers: rhoCentralFoam and sonicFoam. *EPJ Web of Conferences*, 299. <https://doi.org/10.1051/epjconf/202429901005>
2. El-Sayed, A. F. (n.d.). *Aircraft Propulsion and Gas Turbine Engines, Second Edition*.
3. Idris, A. C., Saad, M. R., Zare-Behtash, H., & Kontis, K. (2014). Luminescent measurement systems for the investigation of a scramjet inlet-isolator. *Sensors (Switzerland)*, 14(4), 6606–6632. <https://doi.org/10.3390/s140406606>
4. Jagadish Babu, V., Raje, P., Singh, R., Roy, S., & Sinha, K. (n.d.). Parametric study of the performance of two-dimensional Scramjet Intake. In *18 th Annual CFD Symposium*.
5. Saha, S., & Chakraborty, D. (2012). Hypersonic intake starting characteristics-A CFD validation study. *Defence Science Journal*, 62(3), 147–152. <https://doi.org/10.14429/dsj.62.1340>
6. Sandeep, J., & Gupta, A. V. S. S. K. S. (2025). Assessment of the hypersonic intake isolator and performance evaluation at various flight conditions. *Aerospace Systems*, 8(3), 619–632. <https://doi.org/10.1007/s42401-024-00316-y>